

CMS Draft Analysis Note

The content of this note is intended for CMS internal use and distribution only

2021/11/23

Archive Hash: f903b81-D

Archive Date: 2021/11/23

B meson R_{AA} and Cross Section Ratios in pp and PbPb Collisions at 5.02 TeV

Zhaozhong Shi¹, Maria Faria^{2, 1}, Ran Bi¹, Nuno Leonardo², and Yen-Jie Lee¹

¹Massachusetts Inst. of Technology

² Técnico Lisboa

Abstract

Your abstract here. (One paragraph; max length roughly 200 words (longer will be truncated for EPJC submissions). Absolute max (at arXiv) is 1920 characters.)

This box is only visible in draft mode. Please make sure the values below make sense.

PDFAuthor:	"376"377"000Z"000h"000a"000o"000z"000h"000o"000n"000g"000"040"000S"000h"000i" "000J"000i"000e"000"040"000L"000e"000e
------------	-------------------------------------------------------------------------------------------------------------------------

PDFTitle: "376"377"000B"000"040"000m"000e"000s"000o"000n"000"040"000R"000A"000A"000"04

PDFSubject: "376"377"000C"000M"000S

PDFKeywords: "376"377"000C"000M"000S"000,"000"040"000y"000o"000u"000r"000"040"000t"000o"000

Please also verify that the abstract does not use any user defined symbols

Contents

1	1	Introduction	2
2	2	Datasets, MC samples and event selection	3
3	2.1	Datasets	3
4	2.2	Event Selection	3
5	2.3	MC samples	3
6	2.3.1	MC reweighting	5
7	3	B^+ meson reconstruction	10
8	3.1	Muon and J/ψ selection	11
9	3.2	Track selection	11
10	3.3	J/ψ and ϕ selection	11
11	4	B^+ meson selection	13
12	4.1	Cut optimization	13
13	4.2	Fiducial region	23
14	5	MC-Data Comparison	25
15	5.1	B candidate properties comparison between data and MC	25
16	6	Signal Extraction	27
17	6.1	Closure test of the fitting procedure	30
18	7	Acceptance and Efficiency	32
19	8	Closure Test of the B^+ Corrected Yield	33
20	8.1	Raw Yield Closure	33
21	8.2	Efficiency Closure	33
22	8.3	Corrected Yield Closure	33
23	9	Results	34
24	9.1	p_T differential corrected yield in pp collisions at 5.02 TeV	34
25	9.2	Rapidity differential corrected yield in pp collisions at 5.02 TeV	35
26	9.3	Multiplicity differential corrected yield in pp collisions at 5.02 TeV	35
27	9.4	B_s^0/B^+ ratio as a function of p_T in pp collisions at 5.02 TeV	35
28	9.5	B_s^0/B^+ ratio as a function of y in pp collisions at 5.02 TeV	35
29	9.6	B_s^0/B^+ ratio as a function of Multiplicity in pp collisions at 5.02 TeV	35
30	9.7	B-meson R_{AA} vs p_T at 5.02 TeV	35
31	9.8	B-meson R_{AA} vs y at 5.02 TeV	35
32	9.9	B-meson R_{AA} vs Multiplicity at 5.02 TeV	35
33	10	Systematic uncertainties	36
34	10.1	Summary table	36
35	10.2	T_{AA} and N_{MB}	38
36	10.3	Branching ratio	38
37	10.4	Tracking efficiency	38
38	10.5	Muon efficiency: Tag and Probe	38
39	10.6	MC-Data Discrepancy	41
40	10.7	p_T shape: Bpt weight	42
41	10.8	MC stats: Toy MC study	44
42	10.9	Signal extraction: PDF variation	45
43			

44	A	Non-prompt J/ψ background	46
----	---	------------------------------------------	----

DRAFT

1 Introduction

Relativistic heavy ion collisions allow the study of quantum chromodynamics (QCD) at high energy densities and temperatures. Under such conditions, a state in which quarks and gluons are the relevant degrees of freedom, the quark-gluon plasma (QGP) [? ?], is formed [?] as predicted by lattice QCD calculations [?]. Multiple probes are necessary for characterizing the properties of the QGP medium. Among these, heavy quarks, which are abundantly produced at the CERN LHC, have the potential of providing novel insights into QCD calculations, serving as probes of the QGP [? ?]. As they traverse the QGP, these hard-scattered partons lose energy by means of elastic collisions and medium-induced gluon radiation [? ? ? ?]. The study of parton energy loss can provide insights into the energy density and diffusion properties of the QGP. The full reconstruction of beauty and charm gives access to their four-momenta and allows the study of the flavor and mass dependences of such processes.

In particular, beauty quarks are considered as a golden hard probes to study the transport properties of QGP. Beauty quarks are pre produced in the early stage of heavy-ion collisions. They retain their identities and traverse through the QGP before hadronization and decay. They record the entire evolution of the QGP. From the studies of the production cross sections and nuclear modification factor of b hadrons cross section in pp and heavy-ion collisions, we can understand the energy loss mechanism of beauty quarks in the QGP medium. From the ratios of the production yield of Λ_b and B_s^0 to B^+ from low multiplicity pp, to PbPb, we can understand the beauty hadronization mechanism from small to large systems and test the QCD factorization theorem. These, along with the studies of charm and light flavor hadrons, will allow us to understand the flavor dependence of energy loss and probe the microscopic structure of QGP.

In this analysis, we will perform the measurements of B_s^0 and B^+ cross section as functions of transverse momentum, rapidity, and event multiplicity and within the CMS acceptance $|y| < 2.4$ over a broad range in pp collisions at $\sqrt{s_{NN}} = 5.02$ TeV with the CMS detector. We will use the 2017 pp datasets corresponding to an integrated luminosity of 302.3 pb^{-1} . We will follow the procedures of CADI HIN-17-008 and HIN-19-011 for the analysis. The decay channel we choose for B^+ and B_s^0 measurements are $B_s^0 \rightarrow J/\psi \phi \rightarrow \mu^+ \mu^- K^+ K^-$ and $B_s^0 \rightarrow J/\psi K^+ \rightarrow \mu^+ \mu^- K^+$. We will use the 2018 PbPb B_s^0 and B^+ measurements to obtain the nuclear modification factor and B_s^0/B^+ ratios in pp and PbPb collisions. Our results will be important to help interpret other heavy flavor experimental results and constrain theoretical model calculations.

2 Datasets, MC samples and event selection

2.1 Datasets

This analysis is performed using the **Ultra Legacy** 2017 pp data at $\sqrt{s_{NN}}=5.02$ TeV, which has an integrated luminosity of 302.3 pb^{-1} . The analysis uses the dimuon primary datasets (*DoubleMu* PD). The full name of the used datasets can be found in Table 1.

Table 1: List of pp HLT datasets and triggers with the corresponding integrated luminosities used in the analysis.

System	Primary dataset	Trigger	Luminosity
pp	/DoubleMuon/Run2017G-09Aug2019_UL2017-v1/AOD	HLT_HIL3Mu0NHitQ10_L2Mu0_MAXdR3p5_M1to5_v1	302.3 pb^{-1}

The pp analysis codes are running under the CMSSW_9_4_10 version, and the global tag (GT) used for processing these samples is 94X_dataRun2_ReReco_EOY17_v6.

Events used in the measurement are collected with a trigger requiring the presence of two independent muon candidates. No selection is applied on momentum (including transverse momentum) or pseudo-rapidity. A list of the various triggers with the corresponding integrated luminosities can be found in Table Tab. 1. The pp paths had different prescale values in different runs during the data taking period. A complete description of the di-muon datasets and HLT triggers can be found in [?].

Muon JSON file is applied to filter the pp dataset. It can be found at: Cert306546 – 306826₅TeV_EOY2017ReReco

2.2 Event Selection

To extract pure collision events, several offline selections are applied to each event:

- `pPPrimaryVertexFilterNew`: Events are required to have at least one reconstructed primary vertex. The primary vertex is formed by two or more associated tracks and is required to have a distance from the nominal interaction region of less than 15 cm along the beam axis and less than 0.15 cm in the transverse plane.
- `HBHENoiseFilterResult`: An additional selection of hadronic collisions is applied by requiring a coincidence of at least 2 HF calorimeter towers, with more than 4 GeV of total energy, from the HF detectors on both sides of the interaction point.
- `pBeamScrapingFilterNew`: In addition to HF coincidence, a cluster compatibility filter is used
- `HLT_HIL1DoubleMu0_v1New`: dimuon triggered events

In addition, we also require the absolute value of the z-component of the primary vertex position to be $|PV_z| < 15 \text{ cm}$.

2.3 MC samples

The pp sample is reconstructed using the CMSSW version CMSSW_9_4_10 using the **Ultra Legacy** reconstruction procedures. The global tag used for the production is 94X_mc2017_realistic_forpp for pp samples. Dedicated pp B_s^0 samples were generated in order to estimate the acceptance and selection efficiencies, to study the background components, and to evaluate systematic uncertainties. PYTHIA8 Tune CUETPM8 [? ?], set to generate inclusive (all quark/antiquark, as well as gluon initiated) QCD processes, was used to generate at 5.02 TeV the signal. Several prefilters at the generation steps are applied in order to optimize the generation process

and conserve resources. Only signal events were kept with at least one B_s^0 (forced to decay through the channel $B_s \rightarrow J/\psi \phi$ by means of the EVTGEN package [?]), with $p_T > 5.0 \text{ GeV}/c$, and $|\eta| < 2.4$. In addition, the J/ψ and ϕ meson, are forced to decay in the two muons and two kaons respectively. Final state radiations (FSR) are generated using PHOTOS [?]. The selected signal is simulated with PYTHIA 8 pp collisions

Around 2.5 million events were generated in 1 $\hat{p}_T > 5$ bin. The list of B_s^0 and B MC simulation samples used are shown below:

- B_s^0 : /BsToJpsiPhi_pThat-5_TuneCP5_5p02TeV_Pythia8/RunIpp5Spring18DR-94X_mc2017_realistic_forppRef5TeV_v1-v4/AODSIM
- B^+ : /BsToJpsiPhi_pThat-5_TuneCP5_5p02TeV_Pythia8/RunIpp5Spring18DR-94X_mc2017_realistic_forppRef5TeV_v1-v4/AODSIM

In addition to the signal samples, inclusive non-prompt J/ψ samples, which include several different B meson decaying to J/ψ channels, were also generated. These samples were used to determine the peaking background appearing in the $\mu \mu K K$ mass spectrum. The following samples were used:

- /Pythia8_BJpsiMM_ptJpsi_00_03_Hydjet_MB/HINppWinter16DR-75X_mcRun2_HeavyIon_v13-v1/AODSIM
- /Pythia8_BJpsiMM_ptJpsi_03_06_Hydjet_MB/HINppWinter16DR-75X_mcRun2_HeavyIon_v13-v1/AODSIM
- /Pythia8_BJpsiMM_ptJpsi_03_06_Hydjet_MB/HINppWinter16DR-75X_mcRun2_HeavyIon_v13_ext1-v1/AODSIM
- /Pythia8_BJpsiMM_ptJpsi_06_09_Hydjet_MB/HINppWinter16DR-75X_mcRun2_HeavyIon_v13-v1/AODSIM
- /Pythia8_BJpsiMM_ptJpsi_06_09_Hydjet_MB/HINppWinter16DR-75X_mcRun2_HeavyIon_v13_ext1-v1/AODSIM
- /Pythia8_BJpsiMM_ptJpsi_09_12_Hydjet_MB/HINppWinter16DR-75X_mcRun2_HeavyIon_v13-v1/AODSIM
- /Pythia8_BJpsiMM_ptJpsi_12_15_Hydjet_MB/HINppWinter16DR-75X_mcRun2_HeavyIon_v13-v1/AODSIM
- /Pythia8_BJpsiMM_ptJpsi_15_30_Hydjet_MB/HINppWinter16DR-75X_mcRun2_HeavyIon_v13-v1/AODSIM
- /Pythia8_BJpsiMM_ptJpsi_30_inf_Hydjet_MB/HINppWinter16DR-75X_mcRun2_HeavyIon_v13-v1/AODSIM

The inclusive non-prompt J/ψ samples are also used in the B^+ analysis to constrain the non-prompt background.

Finally, the following prompt J/ψ samples were used:

- /Pythia8_JpsiMM_ptJpsi_00_03_Hydjet_MB/HINppWinter16DR-75X_mcRun2_HeavyIon_v13-v1/AODSIM
- /Pythia8_JpsiMM_ptJpsi_03_06_Hydjet_MB/HINppWinter16DR-75X_mcRun2_HeavyIon_v13-v1/AODSIM
- /Pythia8_JpsiMM_ptJpsi_03_06_Hydjet_MB/HINppWinter16DR-75X_mcRun2_HeavyIon_v13_ext1-v1/AODSIM
- /Pythia8_JpsiMM_ptJpsi_06_09_Hydjet_MB/HINppWinter16DR-75X_mcRun2_HeavyIon_v13-v1/AODSIM
- /Pythia8_JpsiMM_ptJpsi_06_09_Hydjet_MB/HINppWinter16DR-75X_mcRun2_HeavyIon_v13_ext1-v1/AODSIM
- /Pythia8_JpsiMM_ptJpsi_09_12_Hydjet_MB/HINppWinter16DR-75X_mcRun2_HeavyIon_v13-v1/AODSIM
- /Pythia8_JpsiMM_ptJpsi_12_15_Hydjet_MB/HINppWinter16DR-75X_mcRun2_HeavyIon_v13-v1/AODSIM
- /Pythia8_JpsiMM_ptJpsi_15_30_Hydjet_MB/HINppWinter16DR-75X_mcRun2_HeavyIon_v13-v1/AODSIM
- /Pythia8_JpsiMM_ptJpsi_30_inf_Hydjet_MB/HINppWinter16DR-75X_mcRun2_HeavyIon_v13-v1/AODSIM

2.3.1 MC reweighting

For our MC reweighting, we reweight our MC directly to our data shape in the RECO level. We extract the data raw yield from the unbinned fit and the MC raw yield by count the total number of MC candidates with \hat{p}_T , $PV_{Z'}$, and centrality reweighting. The J/ψ , B^+ , and B_s Gen p_T distribution before and after are shown below on Fig 1

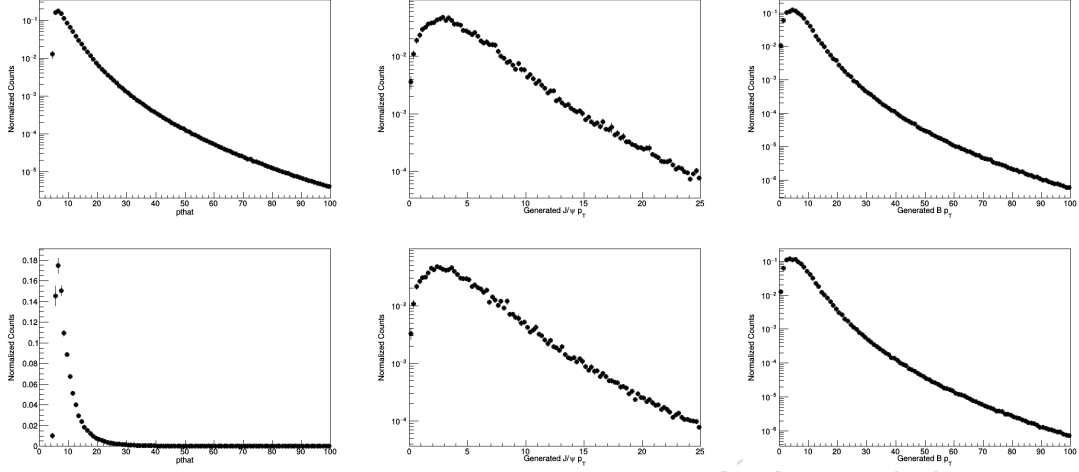


Figure 1: The p_T distribution of the official MC sample (left) as well as the generated J/ψ (middle) and B-meson p_T distribution with p_T weight applied of B^+ and B_s^0 are shown respectively above.

We can see that after \hat{p}_T reweighting, the Gen p_T distributions have become smoother. This validate our \hat{p}_T reweighting procedures.

Then, we take the ratio of the normalized data raw yield to the normalized MC raw yield and perform a fit with function: $y = p_0/x^2 + p_1 \log(x) + p_2$. Our fitting results on spectra ratio are show as follows on Fig 2

The fitting parameters for all functions are shown below on Table 3

Table 2: Summary of fitting parameters for the fitting functions of B^+ and B_s^0 above is shown below.

Particles	p_0	p_1	p_2
B^+	8.65	4.26	-1.48
B_s^0	1.00	0.436	0.171

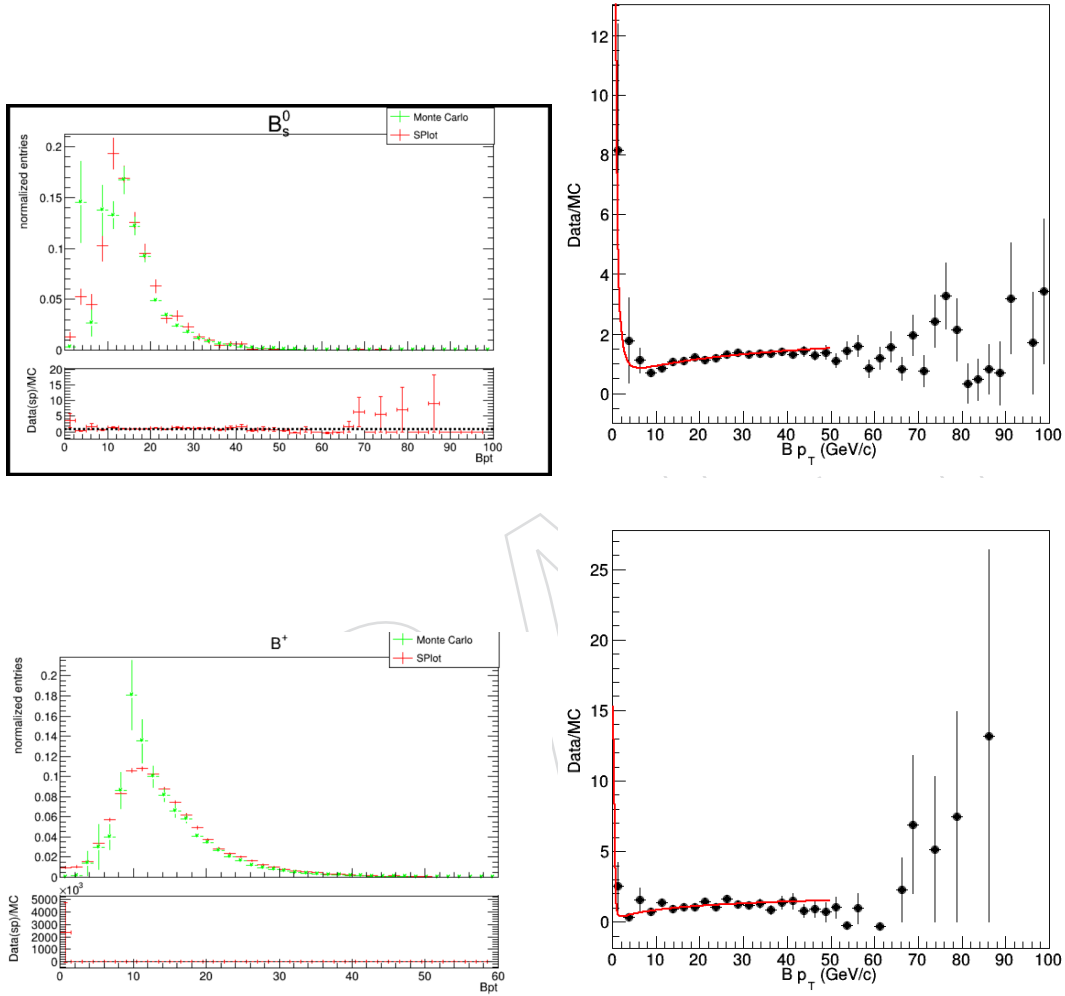


Figure 2: The MC-Data agreement between the signal raw yield in data (red) and MC (green) as a function of B meson p_T for B^+ (up) and B_s^0 (down). We fit the ratio with the function: $y = p_0/x^2 + p_1 \log(x) + p_2$. We will apply this function to the efficiency correct to obtain the systematic uncertainties due to the B p_T shapes.

In addition to above pt shape and centrality reweighting, there must be a primary vertex z position (PVz) reweighting. It is known there will be some non-trivial disagreement on the primary vertex between data and MC simulated with PYTHIA 8. Also, the offsets between data and MC in the X and Y directions are observed in the 2017 pp collisions. A Gaussian fit is applied to both the data and MC PVz distributions, as showed in Fig. 3. The blue markers represent the distribution points for data (left) and MC (middle), while the red lines represents the Gaussian fit results. Add table with fit results Then, the ratio between the two fit results is taken as the weighting function. Finally, we use the ratio function of reweigh the MC and plot the reweighted MC along with the data on the right window. The result after this weighting can be found in Fig. 3 for B^+ (up) and B_s^0 (down). The Gaussian fit results are given by:

Table 3: Summary of fitting parameters for the Gaussian functions ($y = Ne^{\frac{-(x-\mu)^2}{2\sigma^2}}$) of B^+ and B_s^0

Gaussian Fitting Parameters	N	μ	σ
B^+ Data	0.0132	0.7538	6.024
B^+ MC	0.0137	0.6197	5.813
B_s^0 Data	0.0132	0.7539	6.024
B_s^0 MC	0.0137	0.6205	5.815

But note that this analysis is not sensitive to the absolute value of the PV position because the reconstruction of the B_s^0 meson rely only on the relative distance between PV and B_s^0 reconstructed vertex which is presented in the following section.

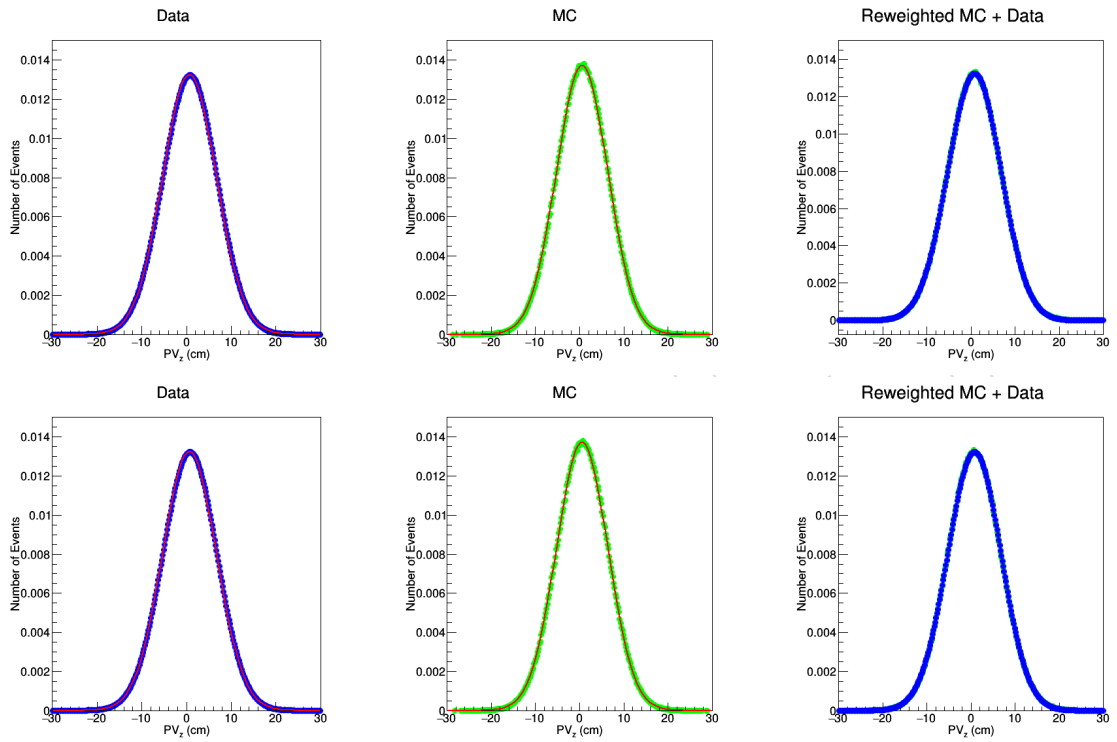


Figure 3: On the left, B_s^0 primary vertex z position (PVz) spectrum obtained in pp data (green marker), fitted with a gaussian function (red line). On the middle, the same but for the MC simulations. On the right is the MC and data after reweighting the MC to data with ratio of data-to-MC Gaussian Fits.

174 In this case, we can see that there is no need to reweight PVz due to the excellent data MC
175 agreement.

DRAFT

3 B^+ meson reconstruction

In this section, the B^+ and B_s^0 mesons reconstruction strategy are presented. The schematic diagram of the workflow is shown in Fig. 4, starting from muons and tracks to B^+ meson candidates. Muon candidates and tracks are required to pass several quality selection criteria as described in Section 3.1 and Section 3.2. J/ψ candidates are reconstructed by vertexing muon pairs with opposite charge, using KinematicConstrainedVertexFitter. The B^+ candidates are built by combining the J/ψ candidates with each of the selected tracks. Finally, a kinematic fit to the J/ψ - K^+ system is performed, forcing the mass of dimuon pair to be equal to the nominal J/ψ mass based on PDG [?]. The selection criteria of the B^+ candidates are described in Section 4.

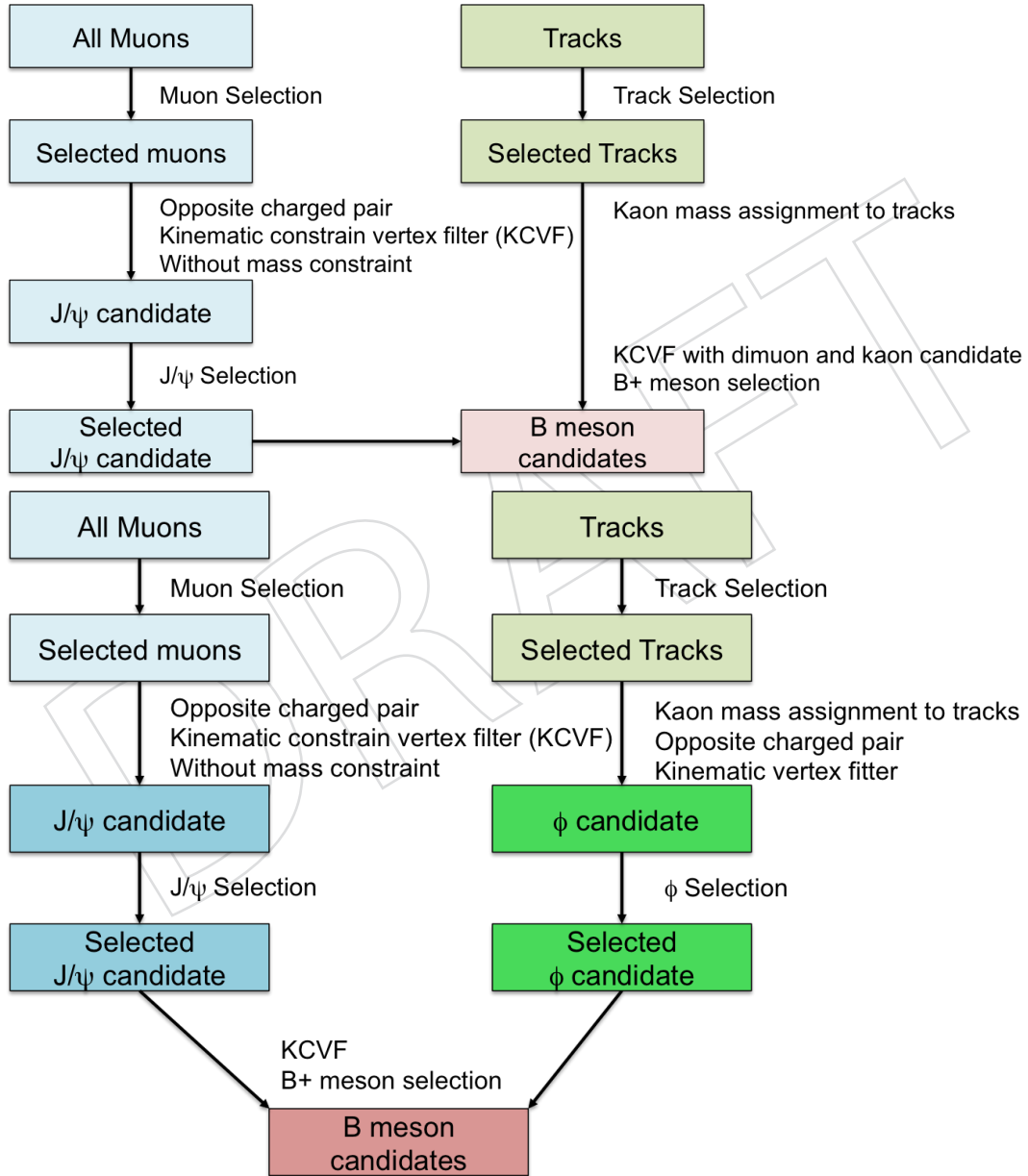


Figure 4: Schematic diagrams of the B^+ meson (top) and B_s^0 reconstruction workflows

3.1 Muon and J/ψ selection

The muon candidates are selected according to the *hybrid-soft muon selection*, developed for the muon analyses on the 2017 5.02 TeV data analyses [?]. It is adapted from the soft-muon ID developed in the BPH group, with two modifications: a) the purity selection is removed, and b) the muon is required to be also global. The *hybrid-soft muon selection* includes the following cuts:

- *isGlobalMuon* and *isTrackerMuon*;
- *isGoodMuon* > 0 ;
- transverse impact parameter $D_{xy} < 0.3$;
- longitudinal impact parameter $D_z < 20$;
- *nPixWMea* > 0 and *nTrkWMea* > 5 (*nPixWMea* and *nTrkWMea* are the number of pixel layers and strips, with valid hits, crossed by a single muon track)

Muons are also requested to fulfill the following acceptance selections:

$$\begin{aligned} p_T^\mu &> 3.5 \text{ GeV}/c && \text{for } |\eta^\mu| < 1.2 \\ p_T^\mu &> (5.77 - 1.89 \times |\eta^\mu|) \text{ GeV}/c && \text{for } 1.2 \leq |\eta^\mu| < 2.1 \\ p_T^\mu &> 1.8 \text{ GeV}/c && \text{for } 2.1 \leq |\eta^\mu| < 2.4 \end{aligned} \quad (1)$$

Muons are required to match specific trigger of the following:

- *Path: HLT_HLT_HIL1DoubleMu0_v1*;
- *Last filter: hltL3f0L3Mu0L2Mu0DR3p5FilteredNHitQ10M1to5 > 0*.

This single muon selection is chosen in order to guarantee a reasonable (above $\approx 10\%$) reconstruction and trigger efficiency for all the selected muons.

In addition to single muon quality selections, for a pair of muon candidates, the following selections are performed:

- the two muons have to have opposite sign;
- dimuon invariant mass has to be within 0.15 GeV from the PDG J/ψ mass;
- probability of the two muon tracks to originate from the same decay vertex $> 1\%$.

3.2 Track selection

Tracks were selected according to the following criteria, as recommended by the HIN tracking group:

- transverse momentum $\text{trkPt} > 0.2$, pseudorapidity $|\eta| < 2.4$;
- relative uncertainty on the track p_T , $(\text{trkPtError}/\text{trkPt}) < 0.1$;
- sum of the numbers of Pixel and Strip hit > 10 ;
- χ^2 probability normalized by number of degrees of freedom and sum of the numbers of Pixel and Strip Layer hit > 0.18 .

3.3 J/ψ and ϕ selection

Finally, we also apply selections on the dimuon and dikaon tracks (for B_s^0 only):

- $|m_{\mu\mu} - m_{J/\psi}| < 0.15 \text{ GeV}/c^2$

- $|m_{K^+K^-} - m_\phi| < 0.015 \text{ GeV}/c^2$

DRAFT

4 B^+ meson selection

The selections described in the previous section (so-called prefilter) are not sufficient to distinguish signal from background, especially at low p_T range where the entire spectrum is dominated by combinatorial backgrounds which arises from random combination of muons and tracks. In order to see clear signals and reduce the uncertainties, several additional selection on the B^+ decay topology were then applied. A cut optimization procedure was performed to decide the cut values. For more details, see Section 4.1.

4.1 Cut optimization

The goal of the optimization procedure is to maximize the figure of merit $S/\sqrt{S+B}$ of the signals while keeping reasonably high signal efficiencies. The optimal cut that minimizes background efficiency for a specific signal efficiency is obtained by the TMVA (Toolkit for Multivariate Data Analysis with ROOT) [?].

Boosted Decision Tree (BDT) is chosen to be the classification method in TMVA training for B^+ . The reconstructed candidates matched to the generated signal in MC sample are used as signal when training, while the reconstructed candidates in sideband ($0.15 \text{ GeV}/c^2 < |M_{B^+} - M_{B^+}^{PDG}| < 0.25 \text{ GeV}/c^2$) of data sample are used as background.

The kinematic variable distributions of daughter tracks and B^+ mesons before and after applying the prefilter is shown on Figure 5, 6, 7, 8



Figure 5: The normalized $J/\psi \mu^-$ kinematic variable distributions before and after prefilter for $p_T = 7 - 10$ GeV/c (left) and $10 - 50$ GeV/c (right) are shown above.



Figure 6: The normalized $J/\psi \mu^+$ kinematic variable distributions before and after prefilter for $p_T = 7 - 10$ GeV/c (left) and $10 - 50$ GeV/c (right) are shown above.



Figure 7: The normalized K^+ track, muons, and K^+ track kinematic variable distributions before and after prefilter for $p_T = 7 - 10$ GeV/c (left) and $10 - 50$ GeV/c (right) are shown above.



Figure 8: The normalized B^+ kinematic variable distributions before and after prefilter for $p_T = 7 - 10$ GeV/c (left) and $10 - 50$ GeV/c (right) are shown above.

We can see that the prefilter cuts do not significantly change the distribution of the kinematic variable shapes and create potential bias. Therefore, these show that our prefilter cut is valid to use.

Then, we use the following six selection variables trained for PbPb:

- dls3D: Normalized decay length (SV PV distance), the distance between primary and B^+ decay (secondary) vertex normalized by its uncertainty
- Balpha: The angle between B^+ meson displacement and B^+ meson momentum in 3D
- Btrk1Pt: Track p_T , the transverse momentum of the track
- Bchi2cl: χ^2 probability, the χ^2 probability of the secondary decay vertex fitting
- Btrk1Eta: The absolute value of the track pseudorapidity
- Btrk1Dxysig: Normalized track Dxy, the transverse distance between track and the primary vertex normalized by its uncertainty

Same thing for B_s^0 . HG

The BDT training setup for all p_T bins are as follows: NTree = 850, MinNodeSize=2.5%, MaxDepth=3, BoostType=AdaBoost, AdaBoostBeta=0.5, UseBaggedBoost, BaggedSampleFraction=0.5, SeparationType=GiniIndex, nCuts=20

The optimal BDT cut values are defined as the numbers which maximize the figure of merit (statistical significance) $S / \sqrt{S + B}$. Here, S is the number of signal in signal region after applying optimal cuts, while B is the number of background in signal region after applying optimal cuts. Signal region is defined as $|M_{B^+} - M_{B^+}^{PDG}| < 0.08 \text{ GeV}/c^2$. For the lowest p_T bin, we used a new figure of merit $S / \sqrt{\gamma_{\text{quantile}}(\alpha/2, S + B, 1)}$ (where, α is chosen to be 1-0.6827) that is suitable for this low signal/background ratio.

- $S = S' \times (\text{signal optimal cut efficiency})$, where S' is the number of signal in signal region before applying optimal cuts.
- $B = B' \times (\text{background optimal cut efficiency})$, where B' is the number of background in signal region before applying optimal cuts.

S' and B' are calculated by fitting the invariant mass plot with prefilter selection, with the same functional form used in the main analysis. However, at the 4 lowest p_T bins, the prefilter is not sufficient to reveal the signal. In those cases, S' is calculated by the expected number of signal from FONLL pp cross-section calculation multiplied by pre-filters efficiency, acceptance from MC, and expected R_{AA} value from previous measurement [?].

Fig. 9 and Fig. 10 show the correlation matrices of the training, in the lowest and highest p_T bin, respectively.



Figure 9: TMVA training correlation matrices of PbPb in p_T 5 - 7 GeV/c.



Figure 10: TMVA training correlation matrices of PbPb in p_T 20 - 50 GeV/c.

273 Fig. 11 shows the overtraining check in the lowest and the highest p_T bin.
 274



Figure 11: TMVA overtraining check of PbPb in p_T 5-7 and 50 - 100 GeV/c, respectively

275 Fig. 12 shows the variable distribution comparison between signal and background, and the
 276 statistical significance curve in p_T 15-20GeV. Some variables show prominently distinct distribu-
 277 tion between signal and background.
 278



Figure 12: TMVA training variable distribution of PbPb in p_T 15 - 20 GeV/c.

279 The maximum significance point is selected as our nominal working point, as shown in Fig. 13.
 280 Tab. 4 shows the summary of the optimal selection criteria in different p_T intervals.
 281 All the other TMVA performance plots not listed in this section are on Appendix. ??.

282

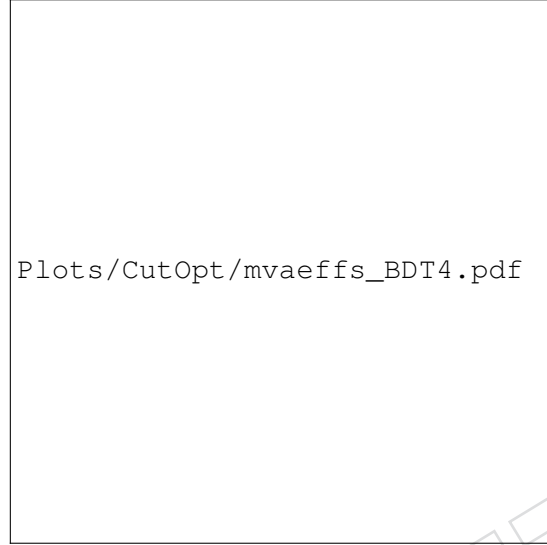


Figure 13: TMVA significance curve of PbPb in p_T 15 - 20 GeV/c.

p_T (GeV/c)	5-7	7-10	10-15	15-20	20-30	30-40	40-50	50-60
BDT	>0.02	>0.03	>0.09	>0.07	>0.10	>0.16	>0.20	>0.27

Table 4: Summary table of selection criteria in different p_T intervals in PbPb collisions

4.2 Fiducial region

As we go to low $B^+ p_T$ where the daughter particles also have predominantly low p_T , it becomes improbable to detect muons in low rapidity ranges due to the limited acceptance of the muons. In other words, the signal and background candidates of B^+ are largely confined to forward rapidity region at low $B^+ p_T$. Fig 14 shows theoretically possible inverse of acceptance, selection efficiency, and total efficiency vs $B^+ p_T$ and $|y|$ 2D distribution with only single muon and track selections but without BDT selections.



Figure 14: The two dimensional maps of the inverse of the acceptance efficiency (left), selection efficiency (middle), and total efficiency (right) vs $B^+ p_T$ and rapidity in MC for the centrality range of 0 - 90% without applying BDT cuts are shown above.

Next, we quantitatively examine the 2D maps of candidate distributions in both data and MC after applying the optimal BDT selections, which are shown in Fig. 15.

It is found that B^+ acceptance is better than B_s^0 , presumably because of less number of tracks needed to reconstruct B meson, which allows broader phase space that the daughter particles can reside. Since this analysis is mainly for the comparison with B_s^0 , we adopted more strict fiducial region ($5 < p_T < 10\text{GeV}$, $1.5 < |y_{lab}| < 2.4$) that is defined using B_s^0 2D map.



Figure 15: B^+ p_T and rapidity two dimensional map of candidates that passed the full analysis cut in data (Left) and MC (right).

5 MC-Data Comparison

5.1 B candidate properties comparison between data and MC

Potential differences between Data and MC distributions of the variables used for the selection of the B^+ signal, can introduce biases in the efficiency corrections. In this section, the distributions of the B^+ selection variables in PbPb data and MC samples are compared.

The Splot method is used for our analysis. This is a likelihood-based method by which we reweight the data using the unbinned fit result. The weights are added to the dataset based on model and yield extraction variables. Each event has two weights: probability of belonging to the signal given its mass, probability of belonging to the background given its mass. The Splot class gives us the distributions of our variables for a given species (signal or background). The advantage of using this method is that we use the full dataset for the comparison in contrast to the sideband subtraction method where one should select the investigation range of signal and background. Furthermore, we use likelihood to describe events' behavior in contrast to the potential misidentification of signal events in background region which might occur in sideband subtraction method. For more details on general description of Splot method applied to this analysis, please refer to the section 4 and 5 of the analysis note CMS AN-19-219([?]).

To show the correlations between the BDT variables to the B^+ invariant mass and validate our Splot techniques approach, we first make the correlation matrices for BDT variables vs B^+ invariant mass Bmass for data and MC as follows in Figure 16:

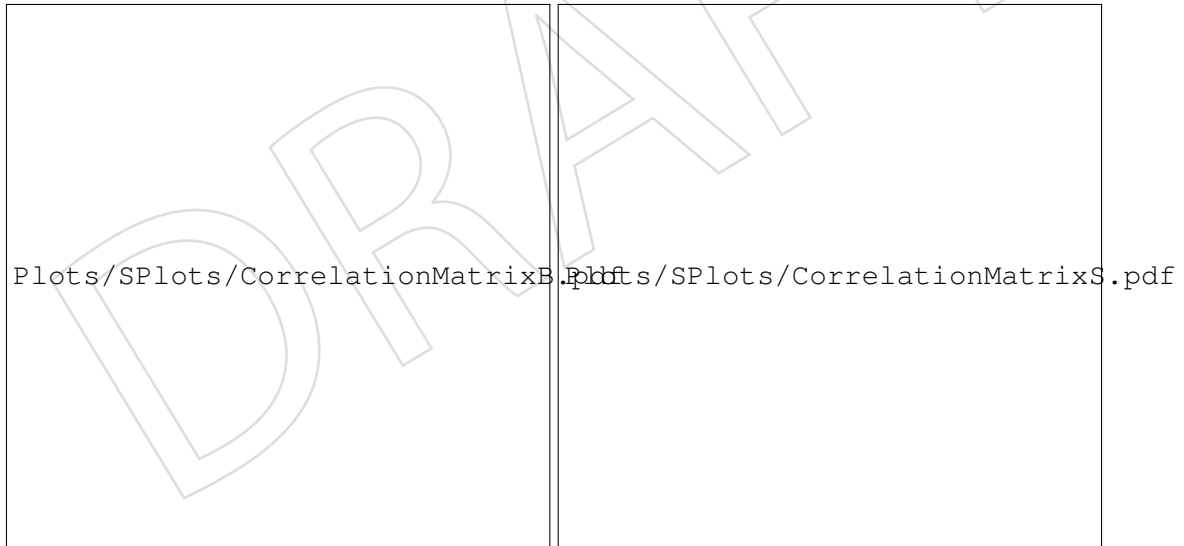
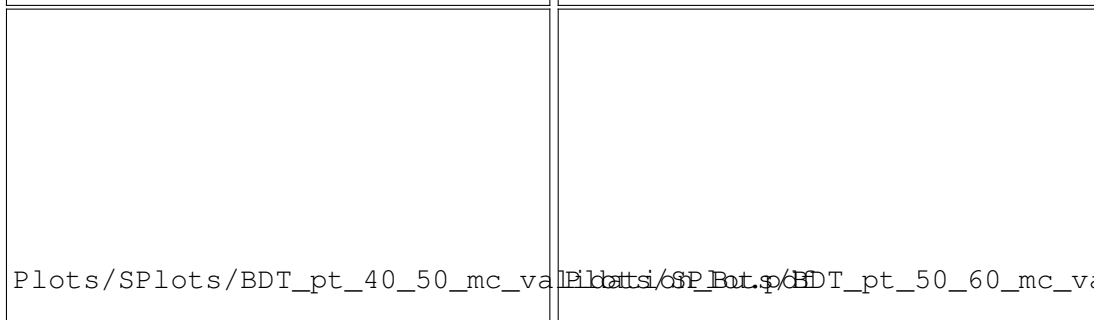
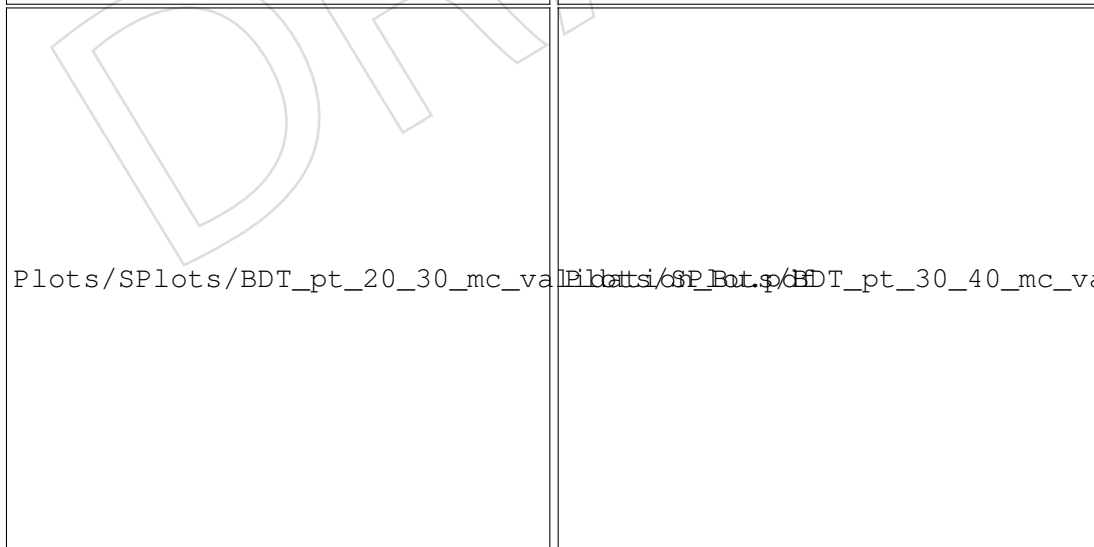
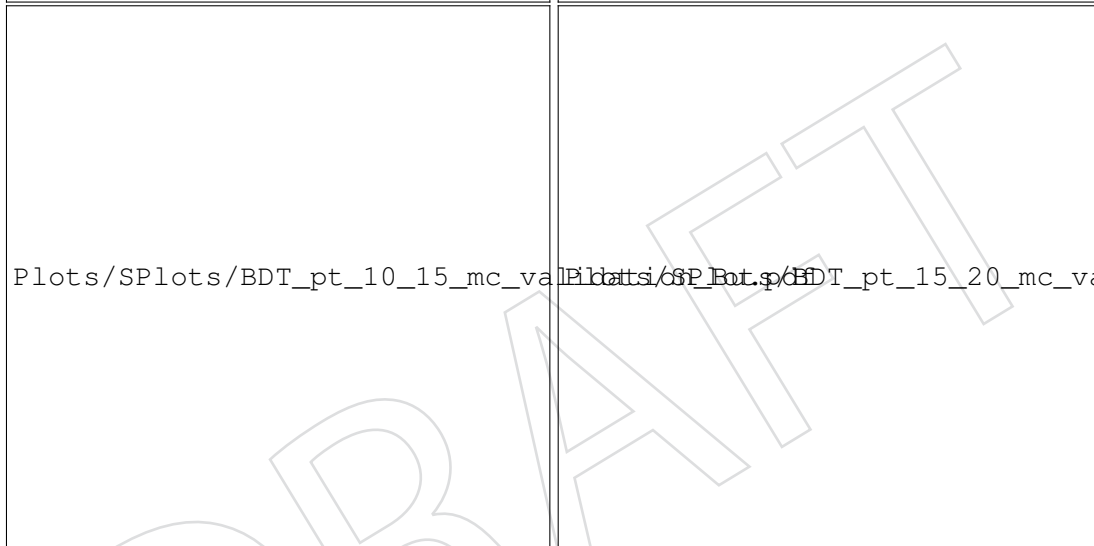
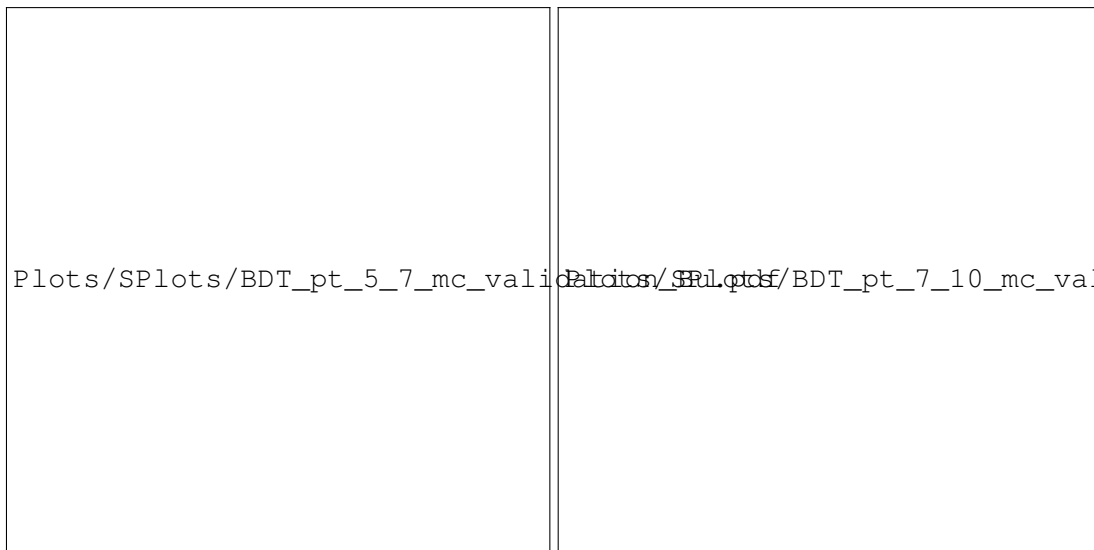


Figure 16: The correlation matrices in data (left) and MC (right) are shown above.

Fig. 17 shows the data and MC comparison results based on Splot method. Here, we focus on BDT values that are directly used in our signal extraction and related to MC distribution validation, rather than the variables themselves used in BDT training. In a wide ranges of BDT, the two distributions show good agreement. We only focus on the region where BDT is greater than the working point and is smaller than the maximum value that candidates have.



6 Signal Extraction

The method and the fit model for signal and background we applied are mostly the same with B_s AN. Please refer to the corresponding section in [?].

However, there is one major difference between B_s and B^+ yield extraction. From the inclusive J/ψ sample study, we have found that there is a clear and sizable contribution from non-prompt J/ψ candidates that are fed down from the B^+ signal in our region of interest. We model this component with an error function and a Gaussian. The error function component mostly comes from 4-prong B meson decay (e.g. $B^+ \rightarrow J/\psi K^*(892)^+$) that are partially reconstructed as $B^+ \rightarrow J/\psi K^+$ (one track is lost) and can form peaking structures for values of the invariant mass below $\approx 5.20 \text{ GeV}/c^2$. The Gaussian contribution mainly comes from $B^+ \rightarrow J/\psi \pi^+$ where pion is misidentified as kaon.

The ratio of the height of error function and the Gaussian is fixed by MC simulation. However, the Gaussian component is shown to be relatively negligible compared to the error function, and even more to the signal double Gaussian of our nominal channel. More details on the non-prompt J/ψ study can be found in Appendix Sec. A.

Note that we do not discriminate B^+ from B^- in raw yield extraction process. Therefore, the invariant mass plots shown below contains both B^+ and B^- signal and backgrounds. This double counting is properly canceled in the corrected yield calculation process later.

In Fig. 18 and Fig. 19, the invariant mass spectra and their pull distributions obtained in the p_T intervals in the PbPb analyses are presented.

We also make the comparison between the symmetric raw yield error and their asymmetric upper and lower yield error using the RooFit framework on the unbinned fit. The table is shown below in Table 5:

Table 5: The comparison between RooFit and unbinned fit framework.

Centrality	p_T (GeV/c)	Raw Yield Error	RawYield Error Up	Raw Yield Error Down
0 - 90%	7 - 10	10.88	11.20	10.66
0 - 90%	10 - 15	20.68	21.05	20.35
0 - 90%	15 - 20	17.86	18.21	17.56
0 - 90%	20 - 50	19.84	20.19	19.55
0 - 30%	10 - 50	27.72	28.01	27.45
30 - 90%	10 - 50	19.53	19.92	19.20
0 - 90%	10 - 50	33.78	34.13	33.47



Figure 18: Invariant mass distribution of B^+ candidates obtained in PbPb collisions in p_T intervals in the transverse momentum range from 7-50 GeV/c and Centrality 0-90%.



Figure 19: Invariant mass distribution of B^+ candidates obtained in PbPb collisions in centrality intervals 0 - 30%, 30 - 90%, and 0 - 90% in the transverse momentum range from 10 - 50 GeV/c.

6.1 Closure test of the fitting procedure

In order to validate the yield extraction procedure, we generate 5000 toy MC for the fit and make the pull distribution. Then we perform the Gaussian fits to the pull distribution to obtain the mean and width. The results are shown in Fig 20 and Fig 21:



Figure 20: The pull distribution and the Gaussian fits for 0 - 90% at 7 - 10, 10 - 15, 15 - 20, 20 - 50 are shown respectively above.



Figure 21: The pull distribution and the Gaussian fits for 0 - 90% at 7 - 10, 10 - 15, 15 - 20, 20 - 50 are shown respectfully above.

351 We can see that all p_T and centrality bins have zero mean and unit width from the Gaussian fits
 352 to the pull distribution. This validate the closure of our fits to extract the B^+ raw yield.

353 7 Acceptance and Efficiency

DRAFT

354 **8 Closure Test of the B^+ Corrected Yield**

355 **8.1 Raw Yield Closure**

356 **8.2 Efficiency Closure**

357 **8.3 Corrected Yield Closure**

DRAFT

9 Results

9.1 p_T differential corrected yield in pp collisions at 5.02 TeV

The method we applied is the same with B_s AN [?].

In Fig. 22, Number of MinBias events-normalized, TAA-normalized, efficiency-corrected and p_T -width divided yield (let's call this "normalized corrected yield") of B^+ mesons in the centrality 0-90% and rapidity region $|y_{lab}| < 2.4$ (Caveat: Note the fiducial region $1.5 < |y_{lab}| < 2.4$ in B^+ p_T 7 - 10GeV/c) in PbPb collisions at $\sqrt{s} = 5.02$ TeV is presented. The boxes around the data points represent the total systematic uncertainties.



Figure 22: B^+ normalized corrected yield vs. p_T in the inclusive centrality range 0-90%. (Left) B^+ analysis p_T bin (Right) B_s^0 analysis p_T bin. Note the fiducial region p_T 5-10GeV and $1.5 < |y_{lab}| < 2.4$

In addition, we provide the normalized corrected yield for inclusive p_T 10-50 GeV/c in 0 - 30%, 30 - 90%, and 0 -90% centrality bins in Fig. 23.

The normalized corrected yields and their uncertainties for various kinematic ranges are summarized in Table. 6 and Table. 7. For more details on systematic uncertainties, see Section. 10.

Table 6: B^+ normalized corrected yields and the uncertainties in various p_T ranges within centrality 0-90%. All the corrected yield values are in units of pb*c/GeV. Note that the global uncertainties are not included here on this table, which are sub 4% level. Note also the fiducial region p_T 5-10GeV and $1.5 < |y_{lab}| < 2.4$ and the same as the B_s p_T binning is reported.

p_T (GeV/c)	Center (GeV/c)	Corr. yield (pb GeV ⁻¹ c)	Stat. up	Stat. down	Syst. up	Syst. down
(7,10)	8.73	331984	15.8%	15.1%	13.6%	13.6%
(10,15)	12.4	298062	7.60%	8.77%	19.1%	19.1%
(15,20)	17.2	66567.7	6.54%	6.66%	7.51%	7.51%
(20,50)	27.3	7730.12	6.64%	5.49%	6.02%	6.02%

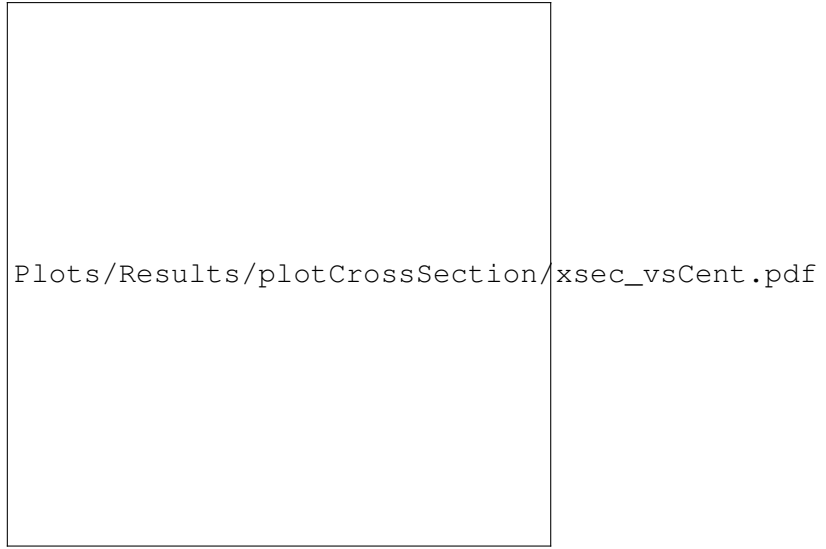


Figure 23: B^+ normalized corrected yield vs. $\langle N_{part} \rangle$ in inclusive p_T . 10-50 GeV is shown above.

Table 7: Summary table of B^+ corrected yield for different centrality bins

Centrality	Corr. yield (pb)	stat. up (+)	stat. down (-)	syst. up (+)	syst. down (-)
0% - 30%	1918800	5.81%	5.54%	16.6%	16.6%
30% - 90%	2481820	8.22%	6.97%	13.6%	13.6%
0 - 90%	2092040	5.06%	4.54%	15.2%	15.2%

9.2 Rapidity differential corrected yield in pp collisions at 5.02 TeV

9.3 Multiplicity differential corrected yield in pp collisions at 5.02 TeV

9.4 B_s^0/B^+ ratio as a function of p_T in pp collisions at 5.02 TeV

9.5 B_s^0/B^+ ratio as a function of y in pp collisions at 5.02 TeV

9.6 B_s^0/B^+ ratio as a function of Multiplicity in pp collisions at 5.02 TeV

9.7 B-meson R_{AA} vs p_T at 5.02 TeV

9.8 B-meson R_{AA} vs y at 5.02 TeV

9.9 B-meson R_{AA} vs Multiplicity at 5.02 TeV

10 Systematic uncertainties

10.1 Summary table

Below are the summary tables of various systematic uncertainties. For detailed description of each systematics source, please refer to the subsequent subsections.

Table 8: Summary of systematic uncertainties from each factor in B^+ PbPb analysis for corrected yield vs p_T . All the values are shown in percentage.

Factors	(7,10)	(10,15)	(15,20)	(20,50)
Hadron tracking efficiency	5%	5%	5%	5%
Data-MC Discrepancy	4.17%	15.25%	3.01%	1.65%
p_T shape	0.162%	0.211%	0.010%	0.008%
PDF variation background	4.46%	2.67%	2.74%	2.36%
PDF variation signal	0.117%	0.546%	0.576%	1.03%
TnP Systematics	6.12%	9.36%	3.28%	0.34%
MC stat.	9.22%	3.36%	1.92%	1.35%
Total	13.59%	19.08%	7.51%	6.02%
N_{MB} events	1.26%	1.26%	1.26%	1.26%
T_{AA}	2.2%	2.2%	2.2%	2.2%
Branching fractions	2.9%	2.9%	2.9%	2.9%
Global Systematics	3.85%	3.85%	3.85%	3.85%

Table 9: Summary of systematic uncertainties from each factor in B^+ PbPb analysis for corrected yield vs centrality. All the values are shown in percentage.

Factors	0 - 30 %	30 % - 90%	0 - 90 %
Hadron tracking efficiency	5%	5%	5%
Data-MC Discrepancy	13.28%	8.49%	11.51%
p_T shape	0.170%	0.106%	0.154%
PDF variation background	0.412%	1.13%	0.427%
PDF variation signal	2.50%	2.57%	2.60%
TnP Systematics	7.20%	7.85%	7.43%
MC stat.	3.37%	2.26%	2.49%
T_{AA}	2.0%	3.6%	2.2%
N_{MB} events	1.26%	1.26%	1.26%
Total	16.63%	13.65%	15.24%
Branching fractions	2.92%	2.92%	2.92%
Global Systematics +)	2.92%	2.92%	2.92%
Global Systematics -)	2.92%	2.92%	2.92%

We also plot the summary plots for the table as follows in Fig 24

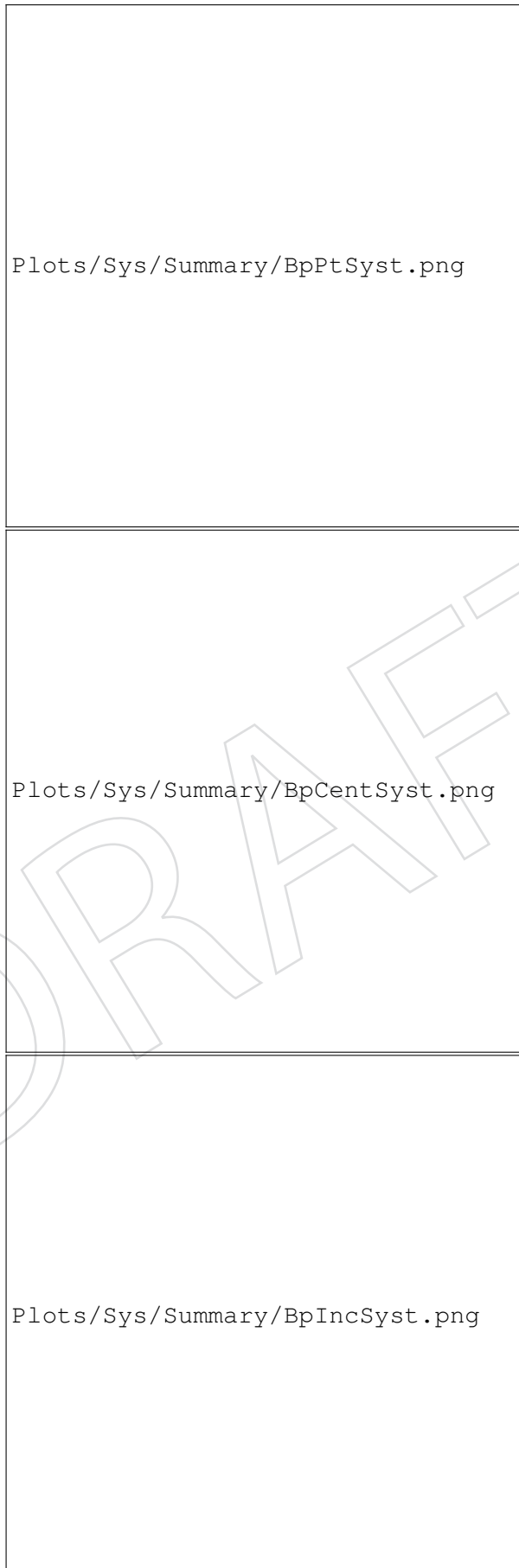


Figure 24: The plots summarizing the systematic uncertainties for p_T bins and centrality bins are shown above.

10.2 T_{AA} and N_{MB}

We use the same uncertainties for T_{AA} (Nuclear overlap function) and N_{MB} (Number of Min-Bias events) listed on the B_s AN [?].

10.3 Branching ratio

The systematic uncertainty on the branching ratio of the decay $B^+ \rightarrow J/\psi K^+$, with $J/\psi \rightarrow \mu^+ \mu^-$, is calculated by adding in quadrature the uncertainties on each sub-channel. The resulting uncertainty for the full decay chain is 2.8% [?]. This is global to all p_T and centrality selections in our analysis.

10.4 Tracking efficiency

The current standard value of tracking efficiency uncertainty for one track is 5% for now, suggested in the link <https://twiki.cern.ch/twiki/bin/viewauth/CMS/HITracking2018PbPb>. This is global to all p_T and centrality selections in our analysis. This number may be updated later.

10.5 Muon efficiency: Tag and Probe

DRAFT

398 The difference between the nominal and varied values are quoted as our systematics, and they
 399 are shown in Figure 25 and Figure 26 and Table. 8 and Table. 9.



Figure 25: The upper bound and lower bound systematic uncertainties in $\langle \frac{1}{\alpha \times \epsilon} \rangle$ vs p_T with total tag and probe correction are shown above.



Figure 26: The upper bound and lower bound systematic uncertainties in $\langle \frac{1}{\alpha \times \epsilon} \rangle$ vs p_T with total tag and probe correction are shown above.

400 According to the studies, we calculate the systematic uncertainties due to tag and probe scale
 401 factor. Table ?? and table ?? summarize the tag and probe systematic uncertainties results for
 402 p_T and centrality from our studies

403 However, according to the Muon POG, due to the issues in the trigger tag and probe scale
 404 factor, we have also conduct the difference between the efficiencies with and without any tag
 405 and probe scale factor correction applied. Our results for p_T and centrality are shown in Figure
 406 ??:

407 The final summary of tag and probe systematic results are shown on Table ?? and ??.

DRAFT

408 **10.6 MC-Data Discrepancy**

DRAFT

10.7 p_T shape: Bpt weight

The potential difference in p_T distributions in data and MC entails difference in calculation of efficiency correction. The B^+ p_T distributions of MC can be modified by Bpt weight (shown in 2.3.1) to have closer distribution with data. The Exponential and Polynomial weight function are given by:

DRAFT

414 We quote the percentage deviation of B p_T weighted efficiency correction factor $\langle 1/(acc \times eff) \rangle$
 415 from the nominal without B p_T weight as the systematic uncertainties. Table. ?? and Table. ??
 416 show the systematics for differential p_T and inclusive p_T , respectively. Fig. ?? and Fig. ?? shows
 417 the comparison plots for differential p_T and inclusive p_T , respectively. Note that the systematics
 418 are very small, thus the differences may not be distinguished prominently on the plots.

419 We can see that the p_T shape systematic uncertainties on the efficiency correction have been
 420 reduced to negligible using the $\langle \frac{1}{\alpha \times \epsilon} \rangle$ approach.

DRAFT

10.8 MC stats: Toy MC study

The statistical uncertainties of $\langle \frac{1}{\alpha \times \epsilon} \rangle$ in MC are examined by toy MC study. From the nominal 2D map, we generated 10000 toy MCs for each rapidity p_T bin. The toy 2D maps are then propagated to the $\langle \frac{1}{\alpha \times \epsilon} \rangle$ data-average calculation. The distribution of data-averages are drawn in each analysis p_T and centrality bin, and the RMS deviation of the distribution (supposedly Gaussian) is compared to the nominal value. The ratio between RMS and the nominal value is quoted as systematics related to MC stats.

Table. ?? and Table. ?? shows the systematics for differential p_T and inclusive p_T , respectively. Fig. ?? and Fig. ?? shows the toy MC $1/(\text{acceptance} \times \text{efficiency})$ distributions for differential p_T and inclusive p_T , respectively. The blue markers are toy MC distribution, the red lines are the nominal correction factors in the main analysis.

DRAFT

10.9 Signal extraction: PDF variation

Here we quote the numbers. For plots with more details, see Appendix. ??.

As discussed in detail in Sec. 6, the central value of the raw yields were extracted using a fit function of Double Gaussian signal and exponential combinatorial background. The non-prompt component was modeled with an error function and a Gaussian peak. The systematic uncertainty on the signal extraction was evaluated by varying the functions used to model the various components:

- Model the signal with a triple Gaussian function.
- Release the constraint on the width of the signal double Gaussian (fixed in the default fit to the MC extracted values). In this case, a scaling factor (a) between the MC widths is left as a free parameter in order to account for possible differences between the resolution in data and MC.
- Fixed the mean of the signal double Gaussian.
- Consider 1st, 2nd, and 3rd order polynomial for combinatorial background.

The detailed description on the release of the constraints on the widths of the signal double Gaussian is as follows. The full signal model used in the fit to data is:

$$\alpha \frac{1}{a\sigma_1\sqrt{2\pi}} e^{-\frac{1}{2} \frac{(B_{mass}-\mu)^2}{(a\sigma_1)^2}} + (1-\alpha) \frac{1}{a\sigma_2\sqrt{2\pi}} e^{-\frac{1}{2} \frac{(B_{mass}-\mu)^2}{(a\sigma_2)^2}}, \quad (2)$$

where a is the resolution scaling factor (the same for both gaussians) which describes the possible discrepancy between data and MC fit, α is the relative proportion between the gaussians, σ_1 and σ_2 are the Gaussians' widths that are directly derived from MC fit, and μ is the mean shared by both Gaussians.

In order to examine the potential systematic difference in data and MC signal fit, we are required to define a moderate variation range of the scaling factor in order not to introduce statistical fluctuations in our estimation. To achieve this, we first performed fit by letting the scaling factor float around in individual p_T bins and inclusive p_T bin (Figure ??). The parameter values from the best fit are summarised in Table ??.

We observed that in several individual p_T bins, the deviations from unity (value for nominal fit) are sizable. In mid p_T bins (10-15-20-30 GeV) where statistics are comparably large, the deviations are small. Whereas in low p_T bins (5-7-10 GeV) and high p_T bins (30-40-50-60 GeV) where statistics are small, the deviations are relatively large. On the other hand, the optimal scaling factors of individual p_T bins agree with that of inclusive p_T bin within a significance of 2σ . From this observation, the sizable differences can be considered to mainly come from statistical limitation of each small p_T ranges. In addition, the 2σ difference can be considered to be the statistical uncertainties of scaling factors of individual p_T bins.

To conclude, we can claim that the scaling factor of the inclusive p_T ($a = 1.09 \pm 0.04$) is a representative of the scaling factor for all p_T bins. Since that factor is an optimal fit parameter, we can take 10% variation from the nominal value (unity) as our signal PDF variation range where the fits are good enough and has reasonably low statistical uncertainties, which is desirable for systematic uncertainties estimation. Here we used jargons increased and decreased width which refers to $a = 1.1$ and 0.9 , respectively.

A Non-prompt J/ψ background

In the B^+ invariant mass spectrum, there are potential background feed-down sources coming from other B meson decays that can form peaking structures in the region of interest, and need to be properly subtracted in order not to bias the yield extraction procedure. In order to estimate these components, we processed the inclusive B meson MC sample with the nominal B^+ channel workflow, and vetoed the candidates that are matched to a genuine B^+ signal. The resulting B candidate mass spectrum in the inclusive p_T range (5-100 GeV/c) is shown in Fig. 27 for PbPb MC samples.

It is clear that these sources create a peaking structure in the region of $M_{\text{inv}} < 5.20 \text{ GeV}/c^2$. This structure can be nicely fit with an error function as done previously in B proton-proton analyses [?]. In addition, there is a minor peak on the right shoulder ($\approx 5.34 \text{ GeV}/c^2$) of the nominal signal ($\approx 5.28 \text{ GeV}/c^2$), and this can be fit with an Gaussian function. There is additional combinatorial background which is fitted with a linear function. This contribution is absorbed in the total combinatorial background of our nominal channel of the main analysis. As described in details in Sec. 6, the shape of the Non-prompt function is used as template in the fit extraction procedure.

Further MC studies were done in order to identify the different channels that give rise to the non-prompt peaking structure in the B^+ invariant mass spectrum. Few main processes were identified:

- 4-body B^+ decays which occur via resonant decay channels e.g. $B^+ \rightarrow J/\psi K^*(892)^+$. In these cases, we distinguish the kaons coming from the $K^*(892)^+$ decays as coming from a signal $B^+ \rightarrow J/\psi K^+$ decay.
- 4-body B^0 decays channels e.g. $B^0 \rightarrow J/\psi K^*(892)^0$.
- $B^+ \rightarrow J/\psi \pi^+$ decays in which we misidentified the π^+ as a K^+ .

The different contributions in PbPb are presented in Fig. 28. The contribution from $B^+ \rightarrow J/\psi \pi$ clearly form a peaking structure on the right shoulder of the nominal decay channel $B^+ \rightarrow J/\psi K^+$. However, the overall magnitude of this component is tiny compared to the other two sources, and negligible compared to the nominal signal. As a consequence, we can barely see the contribution of this peaking structure in the invariant mass plot of B^+ nominal channel.



Figure 27: B^+ candidate mass spectrum obtained in inclusive B meson MC production after vetoing the contribution of genuine B^+ signal candidates in PbPb.

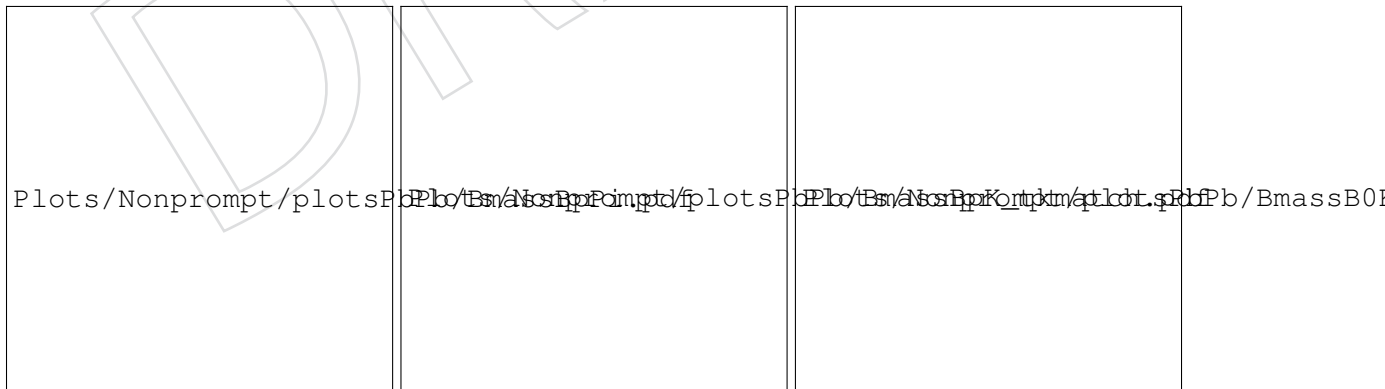


Figure 28: Peaking background contribution from $B^+ \rightarrow J/\psi \pi$ and from K resonant decay channels of B^0 and B^+ in PbPb MC.

499 **Acknowledgments**

500 **References**

DRAFT